Self-Searching Writing of Human-Organ-Scale Three-Dimensional Topographic Scaffolds with Shape Memory by Silkworm-like Electrospun Autopilot Jet

Balchandar Navaneethan and Chia-Fu Chou*

Cite This: *ACS Appl. Mater. Interfaces* 2022, 14, 42841−42851

Read Online

ACCESS | Metrics & More | Article Recommendations | Supporting Information

ABSTRACT: Bioengineered scaffolds satisfying both the physiological and anatomical considerations could potentially repair partially damaged tissues to whole organs. Although three-dimensional (3D) printing has become a popular approach in making 3D topographic scaffolds, electrospinning stands out from all other techniques for fabricating extracellular matrix mimicking fibrous scaffolds. However, its complex charge-influenced jet—field interactions and the associated random motion were hardly overcome for almost a century, thus preventing it from being a viable technique for 3D topographic scaffold construction. Herein, we constructed, for the first time, geometrically challenging 3D fibrous scaffolds using biodegradable poly(ε-caprolactone), mimicking human-organ-scale face, female breast, nipple, and vascular graft, with exceptional shape memory and free-standing

features by a novel field self-searching process of autopilot polymer jet, essentially resembling the silkworm-like cocoon spinning. With a simple electrospinning setup and innovative writing strategies supported by simulation, we successfully overcame the intricate jet—field interactions while preserving high-fidelity template topographies, *via* excellent target recognition, with pattern features ranging from 100's μm to 10's cm. A 3D cell culture study ensured the anatomical compatibility of the so-made 3D scaffolds. Our approach brings the century-old electrospinning to the new list of viable 3D scaffold constructing techniques, which goes beyond applications in tissue engineering.

KEYWORDS: *electrospinning, tissue engineering, self (field)-searching, silkworm-like, 3D scaffolds, PCL, shape memory, human organs*
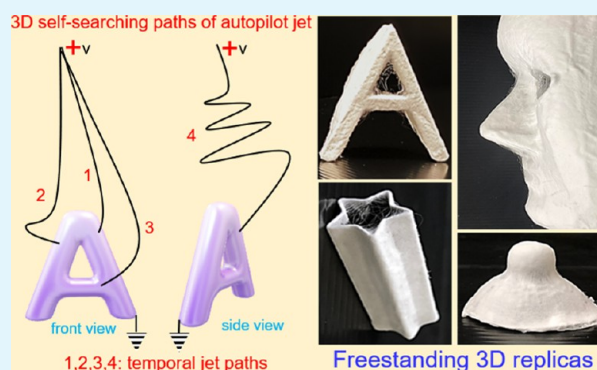
■ INTRODUCTION

Construction of three-dimensional (3D) scaffolds is important for various applications from nano- to macroscale;[1−4] notable examples include functional DNA origami,[5] artificial human organs,[6] 3D-printed houses, and so on.[7] Among these, biomedical applications have attracted intensive attention in recent decades, as genetics and exogenous factors, such as aging, diseases, and injury affecting the human body, highly demand clinical repairs to restore the functions and morphologies of the damaged tissues or organs.[8−10] An ideal engineered construct should resemble the native extracellular matrix (ECM), which is an intricate 3D network composed of collagen fibrils and other biomolecules that mainly provide physical and mechanical strength to the tissue and is responsible for diverse biological functions.[11−14] Currently, molten extrusion-based 3D printing is the only available technique to produce 3D structures with high fidelity and reproducibility for biomedical applications.[7,15−17] In 3D bioprinting, cell and biomaterials are laid in the hydrogel (bioink) form along with the molten synthetic polymer, for example, the FDA-approved poly(ε-caprolactone) (PCL), primarily used for its exceptional mechanical properties and

moderate biodegradability.[18,19] These approaches may have constructed scaffolds of shapes mimicking in part or the organ size; however, they become solid as they cure to yield mechanically inflexible and nonstretchable structures that poorly match the physiological conditions of the human body.[20,21] The computer-controlled motion produced micro-architectures mostly limited to tessellated grid-like patterns and failed to facilitate 3D cell network formation and vascularization as in native tissues, a necessary feature to carry out the essential biophysical and biochemical functions.[18,22−25] Besides, the so-made scaffolds impose high shear stress on cells while occupying a larger area and mass but accommodate lesser cell density, and their poor biodegradability (small
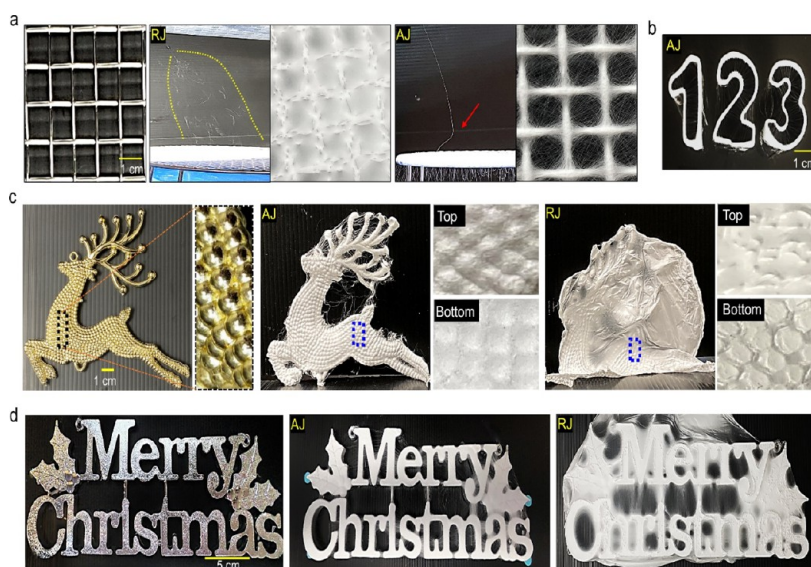
Figure 1. Comparative study of 2D pattern writing resolution by RJ and AJ electrospinning and the associated scaffold replicas. (a) RJ and AJ fiber deposition processes on a "metal grid rack" template, with the yellow dotted lines encompassing the RJ traveling range in air from the needle tip and the "armed jet path" (M1 mode) of the AJ (red arrow). (b) Digital image showing the AJ pattern writing on the "1−2−3" templates. (c) "Reindeer" template with zoomed-in detail of the black dashed box, and the AJ- and the RJ-fabricated replicas taken in a standing position, and their magnified images (from the associated dashed areas, respectively) of both the top and bottom surfaces. (d) AJ- and the RJ-generated patterns on a "Merry Christmas" template.

surface to volume ratio) affects the tissue regeneration and ECM remodeling within these scaffolds.[21,26,27]

Contrary to the sophisticated 3D printing techniques, the cost-effective electrospinning technique produces mechanically flexible fibrous scaffolds effortlessly from a wide range of synthetic and natural polymers and biomaterials that maximally imitate ECM, attributed to the Coulomb force and polymer-instability-driven random jets motion, resulting in nano- to micron-sized fiber diameters (high surface-to-volume ratio).[28−33] However, it was found unfavorable in constructing 3D topographic scaffolds mainly for its poor controllability over the jet path, which is complex and multifactorial, and the lack of adequate structural integrity.[34−38] Altogether, these factors reduced the effectiveness of the strategies employed,[39,40] including technically improved second-generation electrospinning, that is, near-field electrospinning,[41−45] and constrained this technique to only flat (2D) scaffold construction.

Recently, we revealed a novel "autopilot polymer jet" (AJ) electrospinning, in which the AJ may take two distinctive modes in fabricating highly controllable layered-like but "featureless" scaffolds via self-switching of the armed jet motion (M1) and singlet whipping motion (M2) due to the influence of predeposited polymer charge retention or dissipation, respectively.[46] To go beyond previous studies (including ours), here, we demonstrate, for the first time, its writing capability for any challenging 3D topographic scaffolds by introducing innovative strategies, which will be elaborated on in later sections, to make the polymer jet not only self-switch between the M1/M2 modes but also capable of self-searching minimal/optimal field lines (target specificity) adaptive to any complex 3D templates, unattainable by conventional multijet electrospinning (hereafter, referred to as random jets or RJ). The M1 mode may be further elaborated by following a simplified picture using the principle of electrostatics assisted with simulation (Figure S1), which

will help understand the peculiar jet self-searching process on 3D topographies featured in this study. First, the positively charged polymer single jet was driven from the needle tip to the grounded collector along the shortest path where the electric fields are the highest; hence, the fiber was deposited around the center of a planar collector (Figure S1a). The prior deposited fiber, being nonconductive but retaining positive charges before dissipating to the collector, becomes a higher potential area versus the rest of the grounded collector to the incoming polymer jet. Once it formed a locally dense mesh, it repelled the late-coming jet through Coulomb repulsion by pushing it away from the fiber predeposited central region and formed a deflected armed jet (M1 mode) (Figure S1b,c) in depositing fiber now at the periphery (ground) of the central mesh, roughly concentrically extending the size of the mesh planarly or spherically in a 3D fashion if the collector bears a spherical symmetry, as shown later in Figure 4a. However, the potential of the predeposited fibers was constantly modulated, and hence the Coulombic force, with the changing amount of the collected fibers over time and the simultaneous but gradual charge dissipation. Therefore, the charge density in the polymer jet became excessive, which kicked in the mechanical instability by transforming the M1 mode into the whipping motion (M2, not illustrated in the simulation) by more jet stretching/thinning; thus, the surface charge density became lower, that is, minimization of the potential difference in the predeposited fibers while keeping the mass flow conserved. As a result, M2 deposited incoming fibers on the top of the predeposited fibers, with most charge being dissipated. The jet transformed back to M1, as the whipping jet was eventually guided toward the low potential area (peripheral) of the collector due to the same argument above. The whole autopilot process of switching between the M1 and M2 modes, correspondingly increasing the mesh size and thickness, repeats itself indefinitely. Comparative studies are presented wherever possible to discern the conventional wisdom of
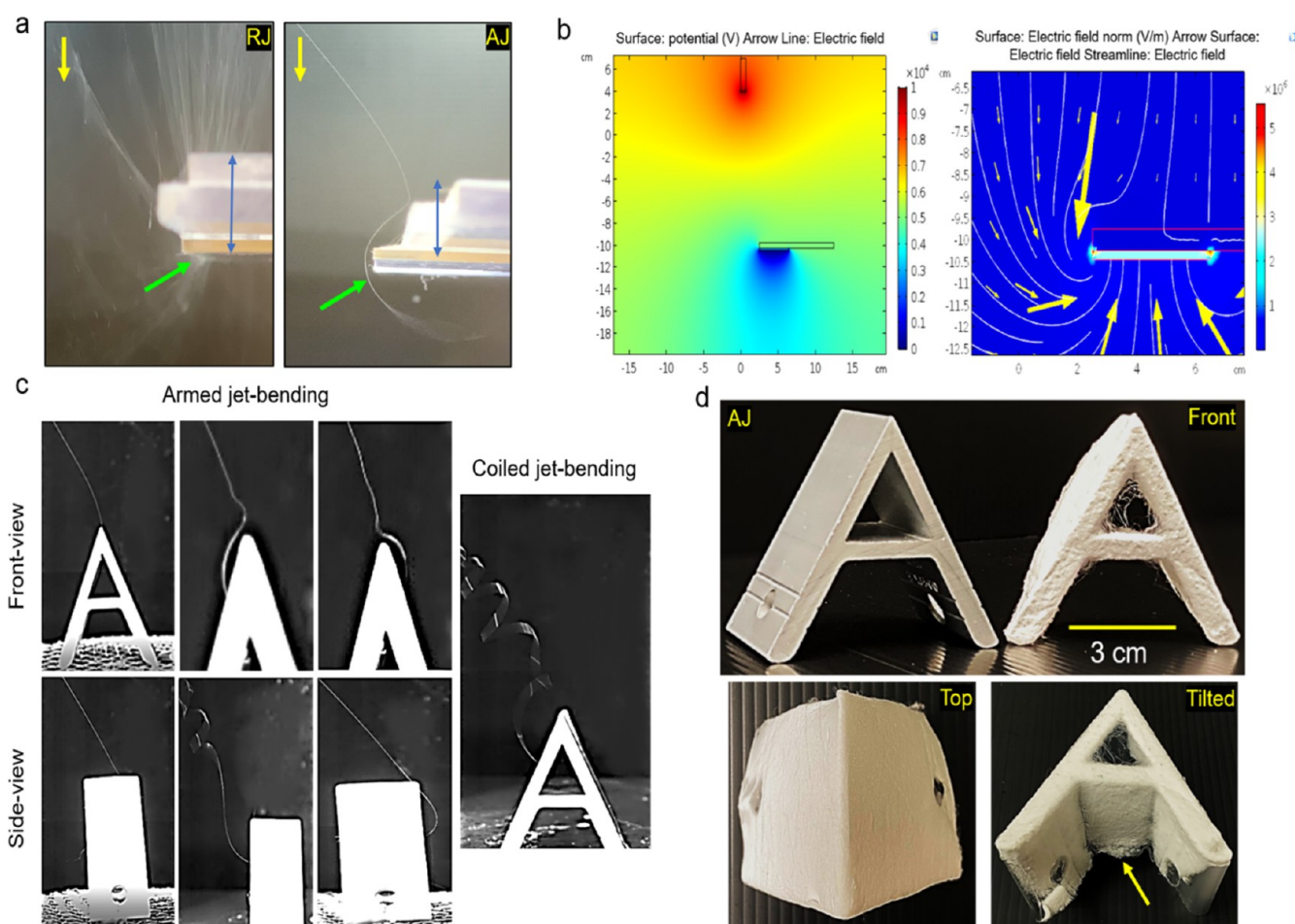
Figure 2. Demonstration of the self-searching process of AJ for 3D scaffold construction. (a) Comparing the fiber deposition of RJ and AJ on a 180°-inversely positioned conducting plate. Magnified image showing the RJ forming fiber bridges on the acrylic/collector template while highly bending (*i.e., self-searching*) AJ depositing fiber only on the downward facing conducting plate. The yellow arrow indicates the direction of the incoming polymer jet from the needle tip. Green and double-blue arrows indicate the position of the conducting plate and acrylic plate, respectively. (b) COMSOL-computed 2D electric potential (left) and field lines (right) between the needle tip (source) and the 180°-inverted stainless-steel conductor as a collector (ground). (c) Images of various armed and coiled jet-bending paths indicating the 3D self-searching process of AJ on coating the A-shape template, shown in the front- and side-view, captured by a high-speed camera (Video S4). (d) Front-, top-, and tilted-view images showing the AJ-produced replica of the A-shape template achieved by combining the self-searching process and novel writing strategies.

strategies by investigating pattern writing resolution, target recognition, replication efficiency, and the structural resiliency (shape memory) in constructing scaffolds of different geometries for potential tissue engineering (TE) applications.

■ RESULTS AND DISCUSSION

2D Pattern Writing. In this study, two different concentrations of PCL solutions (15.78 and 15%) were prepared by dissolving in chloroform (CF)/diethyl ether (DEE) and hexafluoroisopropanol (HFIP), respectively, and were used to generate the (single jet) AJ and (multijet) RJ under the two different optimized electrospinning conditions in the same electrospinning setup. The distinct pattern replication of the AJ on various 2D planar templates is shown first before the 3D scaffold construction to better differentiate it from the conventional RJ process. Figure 1a compares the way fiber deposition is done by both AJ and RJ on a "metal-grid" template shown along with their respective replicas. The RJ splits into multijet, commonly known as *jet-branching*, due to electrostatic repulsion between them, causing it to spray fibers randomly over a large area (several cms) on

the template (Video S1). Parallel electric field lines oriented these fibers in a perpendicular direction to the grids, so they covered the gaps completely, as demonstrated in both theoretical[47] and experimental studies.[48] The AJ, however, deposited fiber as it walked on the grids specifically (Video S2). The central path of the AJ from the needle tip remained virtually nondeviated or much less deviated, where only the jet segments closer to the template got deviated (M1), and with that, it extended the fiber deposition in a circular path peripherally rather than doodling over the template. Subsequently, only a few fibers were seen between the gaps (Figure S2). Figure 1b shows the fiber deposition by AJ on the "1−2−3" templates, of which their wall thickness is 1 mm, demonstrating its fine resolution and high target specificity. In addition, a reindeer template, as shown in Figure 1c, was chosen for showing their vertical (or *z*-axis) writing resolution down to a few hundred microns (Figure S3), in which only the AJ-developed replica carried the topographic details identical to the template with a convex top surface and concave base layer. In contrast, the RJ connected the tiny bumps with fibers horizontally, as evidenced from its flat bottom morphology,
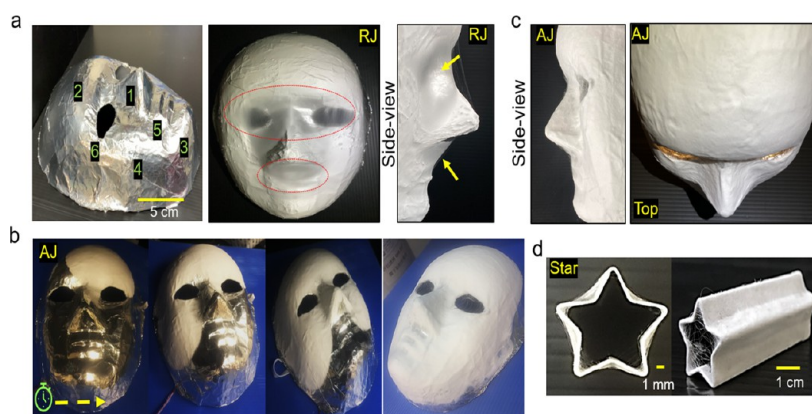
Figure 3. Demonstration of the self-searching process of AJ coupled with different writing strategies for complex 3D scaffold construction. (a) Face mask template with anatomical landmarks is marked by numbers: (1) nose, (2) forehead, (3) chin, (4) cheeks, (5) lip edges, (6) eye sockets, and the RJ-produced replica (front- and side-view) images. Red dotted circles and yellow arrows indicate the slant paths. (b) Sequential images (from left to right) showing the AJ writing area of the "face" scaffold with time. (c) Side- and top-view of the AJ-written replica in (b). (d) Star-shaped replica (front and side views).

similar to its grid template replication (as it got dominated by the field interactions among the bumps), due to its random path and hence the poor resolution. Figure 1d shows the AJ also being able to replicate larger structures of a "Merry Christmas" template with high fidelity.

3D Scaffold Construction. In general, the polymer jet ejecting from the needle tip is shown to be electrostatically attracted to deposit fiber randomly by either a single or multijet on the surface of a collector facing the needle tip (source) (0° or no deflection). On the contrary, the novel self-searching AJ electrospinning process can be elaborated here by a simple experiment design, having a conducting collector facing downward (180° to the front of the needle tip) with the top side stuck to a thick acrylic plate (facing the needle), to study the jet paths of RJ and AJ when reaching the conducting side (Figure 2a). During RJ electrospinning, the multijet sprayed fibers randomly in the air, and shortly, it was unable to establish a stable "Taylor cone" at the needle tip, thereby only dispensing the polymer droplets, indicating the screening of Coulomb attraction by the insulating acrylic plate. Astonishingly, AJ was unaffected, and the jet was seen stretching and bending 180° inversely toward the collector, bypassing the insulating acrylic by following the shortest electric field lines (Figure 2a,b), a feature of the self-searching process, and depositing fibers continuously through the M1/M2 jet-switching (Video S3). In comparison with RJ, AJ experienced a stronger Coulomb force toward the conducting side, which is accountable for its high target specificity as it carries a larger amount of charges due to the nonbranched single jet with a larger diameter, and therefore, the smaller surface area that reduced the amount of solvent evaporation during its flight in air. On the other hand, the optimal viscoelasticity of AJ, determined by the viscosity of the polymer solution and the applied voltage at the needle tip in stretching the solution into the jet, was attributed to the unique 3D jet bending under the electric field (Figure 2b). Evidently, this self-searching process and the 3D adaptation of AJ are the main writing strategies adopted for any challenging 3D templates, as shown in Figure 2b as an example of template "A." The AJ deposited fibers on both outer and inner sides of the top (0°), front (90°), and 180°-inverted sides of a standing "A" through various self-searching 3D jet bending paths (Figure 2c and Video S4), including coiled-jet bending (appears much like M2, but it is

the extensive bending form of the M1, distinguishable by its peripheral fiber deposition), and the maximum jet coverage was achieved on the inner facing sides (Figure 2d, showed by an arrow in the tilted view), when the template was placed in a tilted position on the collector, indicating our writing strategy adopted for complex 3D topography.

Now, we show an even more challenging human-organ-scale 3D template "face," as the topography across the face template is highly nonuniform, and its anatomical landmarks, including nose, forehead, chin, cheeks, lip edges, and eye sockets, represent different heights and curvatures with respect to a planar collector, thus generating feature-dependent field intensity (Figure 3a). Figure 3a (middle) shows the front view of the RJ-developed replica of the face mask. The RJ spreads fibers over an area wide enough to cover one-third of the mask area in a random manner, correspondingly covering the eye openings and failing to deposit fiber on the sites of two intersecting planes, that is, the proximity of the saddle points of a face mask, and instead, they are connected by slopes (indicated by dotted circles and arrows). Also, it piled up fibers at the nose due to its height and high curvature, where the field intensity is high, as shown in the side view. Though the nonconformal deposition also occurred in the AJ case to a lower degree, novel writing strategies accompanying the self-searching process may be implemented to overcome this issue, as stated in the following. The fibers were first deposited only at the nose, and the jet oscillation between the nose and the forehead was observed after the nose tip was covered with fibers, thus connecting them horizontally. These fiber bridges obstruct the AJ from reaching the surfaces beneath the bridges. Similarly, other landmarks were connected by fiber bridges with time, which prevented the AJ from coating fibers on the lower points or surfaces between these features. This issue of nonconformal deposition may be best illustrated with a mirrored L-shaped collector. AJ initially deposited fiber on the top edge of the vertical surface, which is the closest to the source from atop, and then the jet oscillated between the vertical and horizontal surfaces, which are bridged by fibers (hypotenuse side of the template) similar to the scenario between the nose and the forehead due to the equal magnitude of the electric field after shielding as a result of the predeposited fibers on the vertical plane validated by simulation (Figure S4 and Video S5). Apparently, the self-
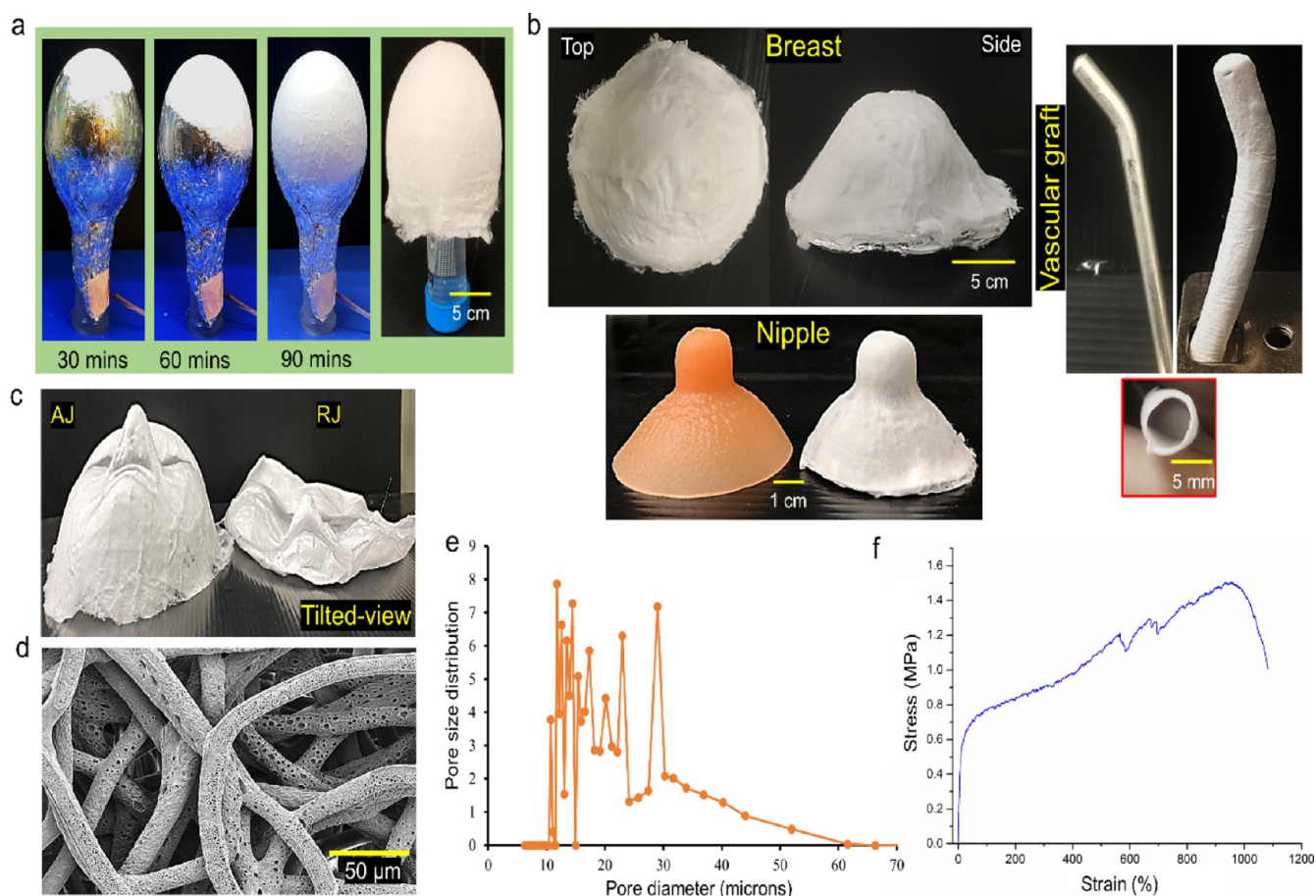
Figure 4. AJ-constructed 3D scaffolds and the associated physical characteristics. (a) Time-lapse images showing the fiber deposition area by AJ on the aluminum foil wrapped round-bottom flask and the pole-supported replica. (b) AJ-produced a breast-mimicking replica (aluminum-foil-covered N95 mask by 3M as a template), female breast nipple adjacent to its silicone nipple template (before coating with conductive spray), and vascular graft replica with a cross-sectional view. (c) Tilted-view of the AJ- and RJ-fabricated replicas without the template support. (d) SEM image of the base layer of the AJ-produced scaffold with buckled fiber morphology. (e) Pore size distribution of the AJ-produced scaffold. (f) Stress *versus* strain curve of the AJ-produced scaffold, indicating the unique progressive extensibility upon stretching.

searching of AJ may not follow a unique path for complex 3D templates since the equivalent paths of the shortest field lines may be implying the need for coupling novel writing strategies to overcome this issue.

We solved this issue by placing the template farther (a few cms away) from the source with its mirrored L-shaped base side facing toward the source (Figure S5 and Video S6) to create asymmetric field paths. AJ experienced stronger Coulomb attraction toward the horizontal plane than the vertical plane as the field intensity becomes weaker with distance away from the source. The AJ taking the M1 mode expanded the fiber deposition area gradually on the horizontal plane from the left to right direction. The fibers covering the horizontal surface, together with the Coulomb repulsion from the deposited fiber, became a high potential zone for AJ (Figure S5d). This distinct potential difference introduced here as a writing strategy is to break the symmetry (equivalence path) of the field lines, thus avoiding the jet oscillation; therefore, both planes were covered from left to right (Figure S5f). Figure 3b shows the process of a 3D face mask writing following this strategy to achieve a conformally complete replica and relatively even thickness (Figure 3c). Alternatively, this suggests that selectively insulating the sides of a collector could resolve the jet oscillation issue to further simplify the construction process with the aid of electrical field stimulation.

In another strategy, as the robustness of AJ was demonstrated with both horizontal and vertical electrospinning setups in our earlier study for the layered-like structures,[46] the template was tilted in the z-axis (topside down) (Figure S6) to guide the jet path to write on the mirrored L-shaped side (mimicking the nostril to the upper lip) with higher accuracy. When coating on a 3D star-shaped template (~1 cm in height), the template rotated clockwise (or counterclockwise) after each V groove was coated to avoid unfavorable jet oscillations between the "V"s (Figure 3d). These strategies showcase leniency of AJ in placement of the template and the importance of its distance, facing direction, and angle on the stage for effective writing of challenging 3D topographies, especially while replicating the outside-facing geometries forming acute angles (below 90°). For instance, the inverted "V" grooves in the star and A-shaped template have angles below 90°, but that obviously did not affect the jet path as they were inside-facing in the same way as an inverted L-shaped collector. The RJ process cannot achieve 3D scaffold writing due to the lack of joint merits of the AJ process discussed above.

Since several parts/organs of humans, for example, breasts, have less complex 3D geometries, that is, without competing for symmetric field lines from multiple local extrusions of the template, replication of those templates requires only the intrinsic self-searching or self-fulfilled process of AJ. To
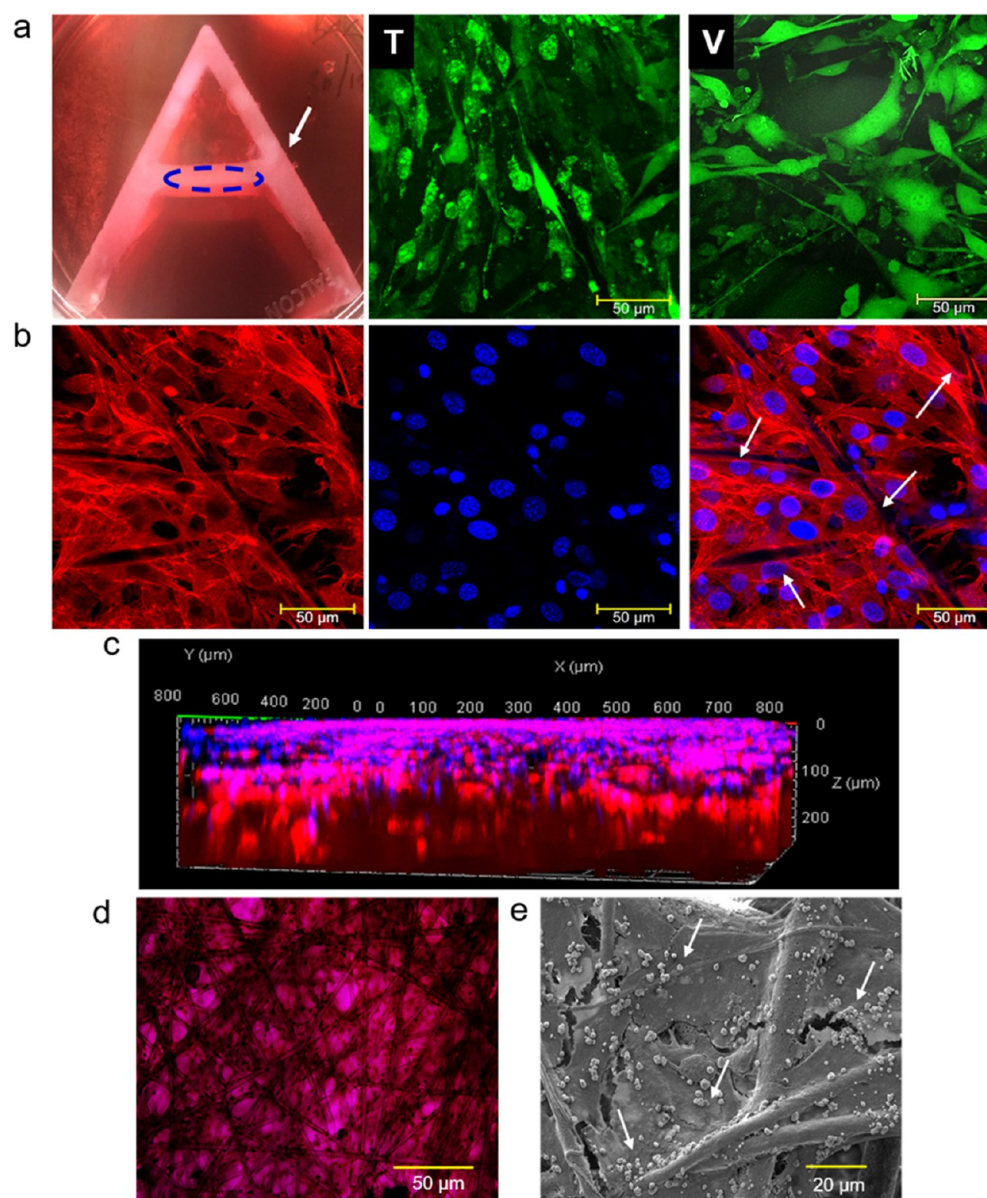
Figure 5. *In vitro* 3D cell culture on AJ-produced scaffolds and cell—scaffold interactions. (a) 3D cell culture of mouse embryonic fibroblasts on the replica "A" (left) and CMFDA live cell images scanned area indicated by a dotted circle (top side, T) and an arrow (vertical side, V) show cell attachment and proliferation into both surfaces of the replica. (b) Left, middle, and right images show the immunostaining of F-actin, nucleus, and their superimposed image, respectively. The presence of electrospun fibers (nonfluorescent) is shown in white arrows. (c) 3D cell penetration depth profile analysis of the fibroblast-seeded AJ-produced scaffold. Confocal fluorescence microscopy shows the depth profile of fibroblast cell penetration (z-depth), which goes deeper than 250 μm (limit by the confocal microscopy) into the scaffold. (d) Sirius red staining image shows the secretion of the ECM by fibroblasts and their cell nuclei along with the nonfluorescent electrospun fibers. (e) SEM image of the ECM-covered electrospun scaffold morphology with tiny rounded residual minerals/salts, indicated by white arrows, formed by the ECM and culture medium.

demonstrate that, we used a round-bottom flask wrapped in aluminum foil positioned upside-down as a template (Figure 4a). RJ laid fiber on the same spot, that is, the pole, throughout the process, so it piled up fibers (Figure S7), but the AJ covered all sides of the sphere from up to down with time, similar to a silkworm cocoon construction (Video S7) without the need of artificially implemented writing strategies. Likewise, shapes mimicking the female breast [aluminum-foil-covered N95 (3M) mask as a template], the nipple and vascular graft of human-scale, and many other 3D shapes were constructed using this "hassle-free process" (Figure 4b and S8).

Characteristics of the AJ-Produced Scaffolds. The real success of our approach in achieving 3D scaffolds goes beyond the conformal fiber deposition on the template by including structural integrity, shape memory, easy separation from the templates, and other aspects that fit TE applications. All the 2D and 3D replicas developed by AJ were smooth, spongy, and free-standing, and their surface morphology/patterns stood firmly, for instance, the 3D face replica (Figure 4c) and the reindeer replica (Figure 1c), even after removal from their respective templates. The following explains the reasons for this. During electrospinning, the high-velocity AJ exerts an axial compression force upon impinging the template and causing it to experience bending in lateral deflection, and as a result, it deposits micron-sized fibers (diameter: 11.5 ± 0.8 μm; n = 15) with buckled morphology (Figure 4d). AJ strikes the template

with higher momentum (larger mass per unit length) *versus* RJ, which helps flatten the semisolid fibers (Figure S9a, indicated by green arrows); thus, it is well conformed with the template's surface to acquire its topographic surface texture. Consequently, the buckled fibers with overlapping junctions fused as drying to retain the shape permanently and increase the bonding strength as well (Figure S9b, indicated by red arrows). The AJ-written replica of the round-bottom flask may be removed and put back into the template easily, owing to the elastic energy stored in the buckled coils that hold the structure by providing exceptional structural resilience (Figure 4a and Video S8), indicating the shape memory of the AJ scaffolds, which would be advantageous when used in physiological conditions. On the contrary, the RJ-produced replicas made up of nanodiameter fibers (diameter: 0.95 ± 0.1 μm; $n = 15$) (Figure S9c) were thin and delicate with uneven thickness and lost their mechanical integrity after separation from their templates (Figures 1b and 4c).

In view of constructing organs having thick walls and solid textures, the thickness of the scaffold was increased up to ~2 mm (Figure S9d), and it can be increased further by extending the fiber deposition time. The porosity result (Figure 4e) indicates that the as-spun thicker scaffold possesses gradient porosity with a wide range of pore size distribution from 10.1 to 61.5 μm, which allows higher cell penetration and *in situ* growth without compromising the mechanical strength described below. The tensile strength analysis of the AJ-produced scaffold showed two necking patterns observed at a strain value of ~584 and 698% in the strain−stress curve (Figure 4f), attributed to the progressive unwinding of buckled coils in the base layer upon stretching. Subsequently, the highest ultimate tensile strength of 1.5 MPa occurred at a high strain value of 957%, and Young's modulus was calculated to be 8.15 MPa, explicitly demonstrating its excellent mechanical stability. A Mullen study was carried out to determine the effect of the pressure generated in the body on the scaffold, that is, physical deformation when implanted. The burst pressure result shows that the mesh can withstand pressures up to 38 mmHg, which is at least 8 times higher than the intraabdominal pressure in a normal adult (~0−5 mmHg).[49] Owing to its highly stretchable nature, the scaffold was seen stretching (expanding) dramatically during the test rather than bursting and exceeding the instrument's maximum limit, only contracting back to restore its original shape partially after the test (Figure S10a). Additionally, a ball-burst strength study was carried out to determine the bursting strength (maximum force) of the scaffolds, which showed a maximum force of 18.36 lbs. To investigate the robustness of the mesh, a 9.0 lbs. weight loaded vertically on the 10 cm diameter scaffold was clipped to the container placed on the orbital shaker rotating at 25 rpm for 30 days. No protrusion was observed after 30 days (Figure S10b). Being porous and mechanically flexible and robust, the AJ-produced scaffolds could significantly reduce the shear-stress generated around them in the host, which greatly reduces the chances of chronic inflammation followed by excessive fibrosis leading to permanent scar tissue formation and other related adverse consequences.[27]

When implanted, it is of utmost importance that the scaffold mimics both the physiological and local anatomical conditions and, at the same time, it should be robust enough to maintain the structural integrity under the physical stress generated in the body.[50−52] Extensive cell culture studies were carried out on various polymeric electrospun scaffolds by various groups in the past. However, the majority of those studies were limited to merely demonstrating the cell attachment and growth only on delicate, plain sheet-like cell-impermeable 2D meshes spun by conventional multijet RJ electrospinning.[38,53] These major drawbacks forbade the electrospinning technique from reaching the next step toward achieving the scaffolds for clinical use for almost two decades. However, the physical and mechanical characteristics results in our study show the excellent robustness and shape memory of the 3D scaffolds along with the anatomical resemblance promising to be a translational approach. While our previous study demonstrated its physiological compatibility, here, an *in vitro* 3D cell culture was carried out to verify its anatomical compatibility *via* multidirectional cell proliferation supported with characterizations of cellular and extracellular compositions on AJ-produced 3D scaffolds by seeding mouse embryonic fibroblasts (3T3) on the top and vertical surface of the A-shaped replica in a tilted position (Figure 5a). Live cell imaging (CMFDA dye) conducted on day 7 showed cell attachment and proliferation on both sides (Figure 5a, middle and right images), which was unaffected by the 3D geometry of the scaffold. The presence of both elongated mature cells and rounded shape daughter cells also indicates an active cell division in the scaffold. Figure 5b shows the immunofluorescence staining images of actin filaments (F-actin) in the plasma membrane and the nucleus of cells. The phalloidin staining shows abundant F-actin expression, which is responsible for cell contraction and migration, and their different orientations reveal 3D cell assembly in the scaffold. The observation of cell nuclei in different sizes from a few microns to 10's of microns in the DAPI staining image supports the results deduced from the live cell imaging. The 3D depth profile shows the cell penetration deeper than 250 μm into the scaffolds (Figure 5c), reaching the z-depth analysis limit set by the nontransparent nature of PCL fibers. The open and interconnected pores and surface pores on the individual fibers help the cells migrate into the scaffold. While the CMFDA and immunofluorescence imaging show the cells morphology, the picrosirius red staining image allows to visualize the collagen expression in ECM secreted by the fibroblast cells, visible in dark pink color, covering more than 90% of surface area (Figure 5d). The hematoxylin nucleus staining also shows the colocalization of the cells in the ECM. Finally, scanning electron microscopy (SEM) image analysis was conducted to investigate the ECM-fiber integration by visualizing the surface morphology. Figure 5e shows that the cells filled the pores (gaps between the fibers) with their matrices and also covered the solvent-induced surface nanopores on the fibers that entirely covered the scaffold surface (the area in the image) with tissue sheets. Overall, the cell culture results indicate that AJ-produced scaffolds are cell-permeable with deep penetration that allow excellent cell attachment, proliferation, and migration, and so they facilitate excellent ECM remodeling and 3D cell network formation as in native ECM, thus promising their usage in TE applications.

■ CONCLUSIONS

In summary, the AJ self-searching writing 3D scaffolds reported in this study indicate a distinct feature occurring only on 3D templates by following the unique motion of 3D self-searching bending paths, which goes beyond M1-M2 switching, thus marking an important paradigm shift that comes as a long-awaited breakthrough in advancing state of the art in the

century-old electrospinning technique. The self-searching feature of AJ surprisingly follows a simple electrostatics principle, analogous to a water stream finding its way through a complex landscape driven by gravity, by orchestrating complicated jet−field interactions, which are persisting issues of the conventional single- and multijet electrospinning in constructing any 3D scaffolds. However, novel writing strategies need to be implemented to overcome the challenges of the field-equivalent multiple extrusions of complex 3D templates, such as the human face. The characterizations performed in this study insinuate that anatomical compatibility was added without compromising the mechanical integrity and physiological compatibility, thus making it deemed for translational applications. The findings presented in this study provide ground for all possible TE applications to be explored by the community using AJ electrospinning from smooth (*e.g.*, skin) to hard (*e.g.*, bone) tissues, reconstructive surgeries, and artificial organ applications. We have also identified a few immediate applications to explore using the AJ-electrospun scaffolds in the near future, but those works are beyond the scope of the current study. Just to name a few applications here that are currently under investigation: (i) the robust 2D replicas of the metal grid rack or diamond-patterned template type inspire us to use them as a bioresorbable pelvic organ prolapse mesh, replacing the controversial permanent polypropylene meshes; (ii) the ability of AJ to transfer minuscule details, demonstrated here with a reindeer template, promises replica fabrication with high fidelity, and the excellent shape memory appears to be an ideal candidate for artificial organ construction and reconstructive surgery, notably the face and breast; (iii) having prepared 3D electrospun scaffolds as a base/contour, feeding a tissue-specific mixture of cell-laden natural biopolymers, for example, hydrogel, into/onto the scaffold may take one step ahead closer toward achieving 3D tissue repairing/regeneration. A simple and flexible setup of the AJ system along with the modular approach, if assisted with automation, may be implemented to assemble individual parts for sophisticated or hierarchical structures, with features superior to 3D printing for commercializable TE applications.

■ EXPERIMENTAL SECTION

Materials. PCL (mw 80,000 kD), CF, DEE, HFIP, direct red 80, picric acid, and Harris's hematoxylin used in this study were purchased from Sigma-Aldrich, USA.

Solution Preparation and Electrospinning. Two different concentrations of PCL solutions (15.78 and 15%) were prepared by dissolving in CF/DEE (volume ratio of 9:1; surface tension of CF and DEE is 26.67 mN/m and 0.2 mN/m at 25 °C) and HFIP (surface tension: 16.14 mN/m at 25 °C), respectively. The 15.78% PCL solution was electrospun to generate AJ based on the preoptimized condition as mentioned in our previous study.[30] In brief, a 22G blunt needle attached to a 15.78% PCL-solution-filled 10 mL syringe was loaded in a syringe pump (Harvard Apparatus, USA) and set to dispense the solution at a rate of 3 mL/h. A 10 kV voltage (Glassman High Voltage, USA) was supplied to cross the needle (positive) and the grounding collector (template), which was placed at a 14 cm distance from the needle tip. The 15% PCL solution was electrospun under the same condition to generate random multijet (RJ), except the template was placed at a 10 cm distance from the needle in order to obtain bead-less fibers. All the experiments were carried out based on the above-mentioned conditions unless otherwise stated. The electrospinning process was recorded using a high-speed camera (Phantom Miro 3, Vision Research, NJ, USA) at 100 frames/s. The silicone breast nipple was coated with Graphite 33 spray (Kontakt Chemie, Belgium) to turn it into an electrically conductive surface,

while all other templates in this study were wrapped with aluminum foil except the mirrored L-shaped conductor (stainless-steel).

Electric Field Simulation. 2D electrostatic potential and field distribution around the model geometry were simulated using COMSOL Multiphysics software. The geometry of the needle (source) and the collector and their separating distances, applied voltage, and permittivity were established according to the experimental conditions. The materials assigned to the boundary, needle, collector, and collected fibers were air, stainless steel, aluminum, and polyethylene (instead of PCL, as it was not found in the COMSOL material library), respectively. The collector was grounded, and the potential on the polyethylene fibers on the collector was set as 1000 and 2000 V for small (2 cm width) and large (4 cm width) fiber meshes, respectively.

Physical Characterization of the Scaffolds. In almost all of the cases, 3D replicas were easily removable from their respective templates from their sides/edges as they do not stick to the templates after the electrospinning process. Fiber morphology of both AJ- and RJ-produced scaffolds was characterized using high-resolution field-emission scanning electron microscopy (FESEM) (JEOL JSM-7900F, Japan) at an accelerating voltage of 5 kV. The fiber samples were sputter coated (JEOL JFC-1200 Fine Coater, Japan) with platinum to convert into the conducting surface prior to imaging under SEM. The mean fiber diameter of samples ($n = 15$) was measured using ImageJ software (NIH, USA). The cross-section of scaffolds was analyzed under an Olympus light microscope, USA. The pore size and pore size distribution in the scaffolds were determined by the wet/dry curve liquid displacing mechanism using a PMI capillary porometer. Mechanical strength analysis was carried out with a tensile tester (Instron, USA). The rectangular strips ($n = 3$) of mesh, 4×1 cm, were placed between the grips, and a load of 1 kN was applied to stretch the mesh at a speed of 10 mm/min. Strain−stress values and Young's modulus were automatically calculated in Instron software. The bursting strength of the scaffolds was analyzed using a low-pressure digital bursting strength tester (QC-116D, Cometech, TW). The 10×10 cm fibrous mesh was tightly clamped with a rubber film. The rubber film swells for the applied hydraulic pressure (95 ± 5 mL/min) in order to detect the maximum pressure strength of the scaffolds. The ball burst strength tester (ISO 9073-5, Cometech, TW) was used to measure the maximum force sustainable by the scaffolds. The 2.5 cm diameter ball head penetrates through the 10×10 cm scaffold at a speed of 100 mm/min, which draws the force−displacement curve.

Scaffold Preparation for the *In Vitro* Cell Culture Study. The replica of "A" and a few other 15 mm circle scaffolds were subjected to oxygen plasma (Harris Plasma cleaner, USA) treatment at 500 mbar for 60 s to turn it hydrophilic for *in vitro* cell culture study and sterilized under UV light for 4 h, followed by soaking in a 10 cm Petri dish supplemented with complete Dulbecco's modified Eagle's medium (DMEM) (10% fetal bovine serum, 1% PS), and then placed in an incubator maintaining 5% CO_2 at 37 °C overnight prior to cell seeding.

***In Vitro* Study.** A liquid nitrogen-frozen vial containing mouse embryonic fibroblasts (3T3) was thawed, and cells were seeded in a 10 cm Petri dish supplemented with complete DMEM and then placed in an incubator. The cells were trypsinized and centrifuged after reaching 70% confluency. The supernatant was discarded, and the cell pellet was disbursed in 1 mL of complete medium. A hemocytometer was used to count the cells by optical microscopy. 10^5 cells were seeded on two sides (top and vertical sides) of the replica "A" for live cell image analysis. The scaffolds subjected to other imaging studies were cut into 15 mm diameter circular shapes, and the same quantity of cells was seeded. The culture medium was replenished with fresh medium every alternative day. All the staining and imaging studies were conducted after 7 days of cell culture, and all the scaffolds were fixed with 4% formaldehyde in phosphate-buffered saline (PBS) solution, except for the live cell imaging study.

Green CMFDA (5-Chloromethylfluorescein Diacetate) Imaging Study. After 7 days of cell culture, portions of the replica seeded with cells were separated using a surgical blade and washed with PBS,

and 180 μL of pure DMEM medium was added to it, followed by the addition of 20 μL of green CMFDA dye (25 μM) (5 μL of CMFDA + 995 μL of pure media) (Thermo Fisher Scientific, USA). The Petri dishes were incubated for 2 h. Then, the medium was removed, and the complete medium was added and incubated overnight. The next day, the medium was removed and washed with PBS for 5 min, then 200 μL of serum-free media was added, and cells were observed under Zeiss Inverted confocal plus super-resolution microscope (LSM 780 plus ELYRA) at 492 nm excitation.

Immunostaining Study. Rhodamine phalloidin and DAPI reagents from Thermo Fisher Scientific were used to stain the actin filaments and nucleus of the fibroblasts. The staining protocols are as follows: in brief, the scaffolds seeded with fibroblasts were fixed with 4% formaldehyde in PBS for 4 h. The scaffolds were washed with PBS after every step throughout the protocol. The scaffolds were soaked with 0.1% Triton X-100 in PBS solution for 5 min, and then 1% bovine serum albumin in PBS was added to the scaffold. After 30 min incubation, 10 μL of Rhodamine phalloidin (20 μM) stock solution was diluted into 200 μL of PBS and incubated at room temperature for 20 min. The scaffolds were then incubated with 200 μL of nucleus staining reagent, that is, DAPI solution (300 nM) for 5 min, followed by PBS wash. Finally, they were air dried and mounted in the ProLong Gold antifade mountant on coverslips and visualized under the confocal microscope (LSM 780 plus ELYRA) at 540 (phalloidin) and 358 nm (DAPI) excitation.

Sirius Red Staining. The cell nucleus and collagen in the ECM were stained with hematoxylin and Direct Red 80 (Sirius red) azo dye, respectively. The formaldehyde-fixed scaffolds were washed with PBS after every incubation step in the following protocol. 200 μL of hematoxylin was added to the coverslips and incubated for 1 h. Then, 250 μL of 0.1% sirius red solution (in saturated picric acid) was added and incubated for 1 h. Finally, the scaffolds were washed with three changes of 100% ethanol and observed under a Leica upright microscope (DM2500M).

FESEM Analysis of Cell-Scaffold Morphology. The scaffolds saved for SEM image analysis were washed with different concentrations of ethanol from low to high (30, 50, 75, 90, and 100%) to dehydrate the cells. Finally, 200 μL of HMDS solution was added to the scaffolds and placed under a laminar flow hood overnight to allow it to evaporate. The dry scaffolds were then sputter coated with gold and scanned under the FESEM at an accelerating voltage of 5 kV.

■ ASSOCIATED CONTENT

Ⓢ Supporting Information

The Supporting Information is available free of charge at https://pubs.acs.org/doi/10.1021/acsami.2c07682.

COMSOL-computed 2D electric potential and field lines, AJ-constructed scaffolds on two different 2D templates, 3D surface profile of the reindeer template, COMSOL-computed results, AJ deposits fiber on the upside-down placed mask, RJ fiber pile up on the round-bottom flask template, various AJ-produced 3D scaffolds on different topographies of 3D templates, fiber morphology analysis of the AJ- and RJ-deposited fibers, and mechanical characteristics of the AJ-produced scaffolds (PDF)

Video showing conventional RJ electrospinning process on a grid template showing a multijet trajectory (MP4)

Video showing AJ electrospinning process on a grid template (MP4)

Video showing AJ self-searching (target specificity) coating process on a 180°-inverted stainless-steel plate (MP4)

Video showing 3D bending paths of AJ self-searching on an A-shaped template (MP4)

Video showing AJ fiber deposition on the hypotenuse side of a mirrored L-shaped conductor (MP4)

Video showing AJ fiber deposition on the inner corner of a mirrored L-shaped conductor (MP4)

Time-lapse movie of the AJ fiber deposition on a 3D round-bottom flask (MP4)

Video showing shape memory of AJ-produced scaffolds (MP4)

■ AUTHOR INFORMATION

Corresponding Author

Chia-Fu Chou − *Institute of Physics and Research Center for Applied Sciences, Academia Sinica, Taipei 11529 Taiwan, R.O.C.;* ⓘ orcid.org/0000-0003-0070-5556; Email: cfchou@phys.sinica.edu.tw

Author

Balchandar Navaneethan − *Institute of Physics and Nano Science and Technology Program, Taiwan International Graduate Program, Academia Sinica, Taipei 11529 Taiwan, R.O.C.; Department of Engineering and System Science, National Tsing Hua University, Hsinchu 30013 Taiwan, R.O.C.*

Complete contact information is available at:
https://pubs.acs.org/10.1021/acsami.2c07682

Author Contributions

B.N. conceived the study. B.N. and C.-F.C. conceptualized the study. B.N. designed experiments, and B.N. and C.-F.C. jointly investigated the experiment's results. C.-F.C. supervised the whole project. B.N. wrote the manuscript. C.-F.C. reviewed and edited the manuscript.

Notes

The authors declare no competing financial interest.

■ ACKNOWLEDGMENTS

■ REFERENCES

(1) Le Fer, G.; Becker, M. L. 4D Printing of Resorbable Complex Shape-Memory Poly(propylene fumarate) Star Scaffolds. *ACS Appl. Mater. Interfaces* **2020**, *12*, 22444−22452.

(2) Elder, B.; Neupane, R.; Tokita, E.; Ghosh, U.; Hales, S.; Kong, Y. L. Nanomaterial Patterning in 3D Printing. *Adv. Mater.* **2020**, *32*, 1907142.

(3) Eom, S.; Park, S. M.; Hong, H.; Kwon, J.; Oh, S.-R.; Kim, J.; Kim, D. S. Hydrogel-Assisted Electrospinning for Fabrication of a 3D Complex Tailored Nanofiber Macrostructure. *ACS Appl. Mater. Interfaces* **2020**, *12*, 51212−51224.

(4) Sharma, C.; Dinda, A. K.; Potdar, P. D.; Chou, C.-F.; Mishra, N. C. Fabrication and characterization of novel nano-biocomposite scaffold of chitosan-gelatin-alginate-hydroxyapatite for bone tissue engineering. *Mater. Sci. Eng., C* **2016**, *64*, 416−427.

(5) Rothemund, P. W. K. Folding DNA to Create Nanoscale Shapes and Patterns. *Nature* **2006**, *440*, 297−302.

(6) Marx, V. Organs from the Lab. *Nature* **2015**, *522*, 373−377.

(7) Murr, L. E. Frontiers of 3D Printing/Additive Manufacturing: from Human Organs to Aircraft Fabrication†. *J. Mater. Sci. Technol.* **2016**, *32*, 987−995.

(8) Atala, A.; Kasper, F. K.; Mikos, A. G. Engineering Complex Tissues. *Sci. Transl. Med.* **2012**, *4*, 160rv12.

(9) Amin, K.; Moscalu, R.; Imere, A.; Murphy, R.; Barr, S.; Tan, Y.; Wong, R.; Sorooshian, P.; Zhang, F.; Stone, J.; Fildes, J.; Reid, A.; Wong, J. The Future Application of Nanomedicine and Biomimicry in Plastic and Reconstructive Surgery. *Nanomedicine* **2019**, *14*, 2679−2696.

(10) HRSA. Organ Procurement and Transplantation Network. https://optn.transplant.hrsa.gov/data/ (accessed on Mar 31, 2022).

(11) Wade, R. J.; Burdick, J. A. Engineering ECM Signals into Biomaterials. *Mater. Today* **2012**, *15*, 454−459.

(12) Khademhosseini, A.; Langer, R. A Decade of Progress in Tissue Engineering. *Nat. Protoc.* **2016**, *11*, 1775−1781.

(13) Gater, R.; Njoroge, W.; Owida, H. A.; Yang, Y. Scaffolds mimicking the native structure of tissues. In *Handbook of Tissue Engineering Scaffolds: Volume One*; Mozafari, M., Sefat, F., Atala, A., Eds.; Woodhead Publishing, 2019; pp 51−71.

(14) Gautam, S.; Chou, C.-F.; Dinda, A. K.; Potdar, P. D.; Mishra, N. C. Surface Modification of Nanofibrous Polycaprolactone/gelatin Composite Scaffold by Collagen Type I Grafting for Skin Tissue Engineering. *Mater. Sci. Eng., C* **2014**, *34*, 402−409.

(15) Bittner, S. M.; Guo, J. L.; Melchiorri, A.; Mikos, A. G. Three-dimensional Printing of Multilayered Tissue Engineering Scaffolds. *Mater. Today* **2018**, *21*, 861−874.

(16) Tejo-Otero, A.; Buj-Corral, I.; Fenollosa-Artés, F. 3D Printing in Medicine for Preoperative Surgical Planning: A Review. *Ann. Biomed. Eng.* **2020**, *48*, 536−555.

(17) Park, S.-H.; Kang, B.-K.; Lee, J. E.; Chun, S. W.; Jang, K.; Kim, Y. H.; Jeong, M. A.; Kim, Y.; Kang, K.; Lee, N. K.; Choi, D.; Kim, H. J. Design and Fabrication of a Thin-Walled Free-Form Scaffold on the Basis of Medical Image Data and a 3D Printed Template: Its Potential Use in Bile Duct Regeneration. *ACS Appl. Mater. Interfaces* **2017**, *9*, 12290−12298.

(18) Kang, H.-W.; Lee, S. J.; Ko, I. K.; Kengla, C.; Yoo, J. J.; Atala, A. A 3D Bioprinting System to Produce Human-scale Tissue Constructs with Structural Integrity. *Nat. Biotechnol.* **2016**, *34*, 312−319.

(19) Do, A.-V.; Khorsand, B.; Geary, S. M.; Salem, A. K. 3D Printing of Scaffolds for Tissue Regeneration Applications. *Adv. Healthcare Mater.* **2015**, *4*, 1742−1762.

(20) Xie, Z.; Gao, M.; Lobo, A. O.; Webster, T. J. 3D Bioprinting in Tissue Engineering for Medical Applications: The Classic and the Hybrid. *Polymers* **2020**, *12*, 1717.

(21) Kačarević, Ž. P.; Rider, P. M.; Alkildani, S.; Retnasingh, S.; Smeets, R.; Jung, O.; Ivanišević, Z.; Barbeck, M. An Introduction to 3D Bioprinting: Possibilities, Challenges and Future Aspects. *Materials* **2018**, *11*, 2199.

(22) Sydney Gladman, A.; Matsumoto, E. A.; Nuzzo, R. G.; Mahadevan, L.; Lewis, J. A. Biomimetic 4D Printing. *Nat. Mater.* **2016**, *15*, 413−418.

(23) Subbiah, R.; Hipfinger, C.; Tahayeri, A.; Athirasala, A.; Horsophonphong, S.; Thrivikraman, G.; França, C. M.; Cunha, D. A.; Mansoorifar, A.; Zahariev, A.; Jones, J. M.; Coelho, P. G.; Witek, L.; Xie, H.; Guldberg, R. E.; Bertassoni, L. E. 3D Printing of Microgel-Loaded Modular Microcages as Instructive Scaffolds for Tissue Engineering. *Adv. Mater.* **2020**, *32*, 2001736.

(24) Bertassoni, L. E. Bioprinting of Complex Multicellular Organs with Advanced Functionality-Recent Progress and Challenges Ahead. *Adv. Mater.* **2022**, *34*, 2101321.

(25) Ma, Y.; Hu, N.; Liu, J.; Zhai, X.; Wu, M.; Hu, C.; Li, L.; Lai, Y.; Pan, H.; Lu, W. W.; Zhang, X.; Luo, Y.; Ruan, C. Three-Dimensional Printing of Biodegradable Piperazine-Based Polyurethane-Urea Scaffolds with Enhanced Osteogenesis for Bone Regeneration. *ACS Appl. Mater. Interfaces* **2019**, *11*, 9415−9424.

(26) Miao, S.; Castro, N.; Nowicki, M.; Xia, L.; Cui, H.; Zhou, X.; Zhu, W.; Lee, S.-j.; Sarkar, K.; Vozzi, G.; Tabata, Y.; Fisher, J.; Zhang, L. G. 4D Printing of Polymeric Materials for Tissue and Organ Regeneration. *Mater. Today* **2017**, *20*, 577−591.

(27) Murphy, S. V.; De Coppi, P.; Atala, A. Opportunities and Challenges of Translational 3D Bioprinting. *Nat. Biomed. Eng.* **2020**, *4*, 370−380.

(28) Yoshimoto, H.; Shin, Y.; Terai, H.; Vacanti, J. A Biodegradable Nanofiber Scaffold by Electrospinning and its Potential for Bone Tissue Engineering. *Biomaterials* **2003**, *24*, 2077−2082.

(29) Gautam, S.; Dinda, A. K.; Mishra, N. C. Fabrication and Characterization of PCL/gelatin Composite Nanofibrous Scaffold for Tissue Engineering Applications by Electrospinning Method. *Mater. Sci. Eng., C* **2013**, *33*, 1228−1235.

(30) Spasova, M.; Stoilova, O.; Manolova, N.; Rashkov, I. Electrospun PLLA/PEG scaffolds. *Mater. Today* **2019**, *28*, 114−115.

(31) Xue, J.; Wu, T.; Dai, Y.; Xia, Y. Electrospinning and Electrospun Nanofibers: Methods, Materials, and Applications. *Chem. Rev.* **2019**, *119*, 5298−5415.

(32) Rahmati, M.; Mills, D. K.; Urbanska, A. M.; Saeb, M.; Venugopal, J. R.; Ramakrishna, S.; Mozafari, M. Electrospinning for Tissue Engineering Applications. *Prog. Mater. Sci.* **2021**, *117*, 100721.

(33) Chaurey, V.; Block, F.; Su, Y.-H.; Chiang, P.-C.; Botchwey, E.; Chou, C.-F.; Swami, N. S. Nanofiber Size-dependent Sensitivity of Fibroblast Directionality to the Methodology for Scaffold Alignment. *Acta Biomater.* **2012**, *8*, 3982−3990.

(34) Reneker, D. H.; Yarin, A. L.; Fong, H.; Koombhongse, S. Bending Instability of Electrically Charged Liquid Jets of Polymer Solutions in Electrospinning. *J. Appl. Phys.* **2000**, *87*, 4531−4547.

(35) Yarin, A. L.; Koombhongse, S.; Reneker, D. H. Bending Instability in Electrospinning of Nanofibers. *J. Appl. Phys.* **2001**, *89*, 3018−3026.

(36) Reneker, D. H.; Yarin, A. L. Electrospinning Jets and Polymer Nanofibers. *Polymer* **2008**, *49*, 2387−2425.

(37) Collins, G.; Federici, J.; Imura, Y.; Catalani, L. H. Charge Generation, Charge Transport, and Residual Charge in the Electrospinning of Polymers: A Review of Issues and Complications. *J. Appl. Phys.* **2012**, *111*, 044701.

(38) Khorshidi, S.; Solouk, A.; Mirzadeh, H.; Mazinani, S.; Lagaron, J. M.; Sharifi, S.; Ramakrishna, S. A Review of Key Challenges of Electrospun Scaffolds for Tissue-engineering Applications. *J. Tissue Eng. Regener. Med.* **2016**, *10*, 715−738.

(39) Lee, J.; Lee, S. Y.; Jang, J.; Jeong, Y. H.; Cho, D.-W. Fabrication of Patterned Nanofibrous Mats Using Direct-Write Electrospinning. *Langmuir* **2012**, *28*, 7267−7275.

(40) Arras, M. M. L.; Grasl, C.; Bergmeister, H.; Schima, H. Electrospinning of Aligned Fibers with Adjustable Orientation Using Auxiliary Electrodes. *Sci. Technol. Adv. Mater.* **2012**, *13*, 035008.

(41) Kameoka, J.; Orth, R.; Yang, Y.; Czaplewski, D.; Mathers, R.; Coates, G. W.; Craighead, H. G. A Scanning Tip Electrospinning Source for Deposition of Oriented Nanofibres. *Nanotechnology* **2003**, *14*, 1124−1129.

(42) Sun, D.; Chang, C.; Li, S.; Lin, L. Near-Field Electrospinning. *Nano Lett.* **2006**, *6*, 839−842.

(43) Chen, H.; Malheiro, A. d. B. F. B.; van Blitterswijk, C.; Mota, C.; Wieringa, P. A.; Moroni, L. Direct Writing Electrospinning of Scaffolds with Multidimensional Fiber Architecture for Hierarchical Tissue Engineering. *ACS Appl. Mater. Interfaces* **2017**, *9*, 38187−38200.

(44) Jordahl, J. H.; Solorio, L.; Sun, H.; Ramcharan, S.; Teeple, C. B.; Haley, H. R.; Lee, K. J.; Eyster, T. W.; Luker, G. D.; Krebsbach, P.

H.; Lahann, J. 3D Jet Writing: Functional Microtissues Based on Tessellated Scaffold Architectures. *Adv. Mater.* **2018**, *30*, 1707196.

(45) Li, X.; Li, Z.; Wang, L.; Ma, G.; Meng, F.; Pritchard, R. H.; Gill, E. L.; Liu, Y.; Huang, Y. Y. S. Low-Voltage Continuous Electrospinning Patterning. *ACS Appl. Mater. Interfaces* **2016**, *8*, 32120−32131.

(46) Navaneethan, B.; Vijayakumar, G. P.; Ashang Luwang, L.; Karuppiah, S.; Jayarama Reddy, V.; Ramakrishna, S.; Chou, C.-F. Novel Self-Directing Single-Polymer Jet Developing Layered-Like 3D Buckled Microfibrous Scaffolds for Tissue Engineering Applications. *ACS Appl. Mater. Interfaces* **2021**, *13*, 9691−9701.

(47) Gupta, A.; Ayithapu, P.; Singhal, R. Study of the Electric Field Distribution of Various Electrospinning Geometries and its Effect on the Resultant Nanofibers using Finite Element Simulation. *Chem. Eng. Sci.* **2021**, *235*, 116463.

(48) Chaurey, V.; Chiang, P.-C.; Polanco, C.; Su, Y.-H.; Chou, C.-F.; Swami, N. S. Interplay of Electrical Forces for Alignment of Sub-100 nm Electrospun Nanofibers on Insulator Gap Collectors. *Langmuir* **2010**, *26*, 19022−19026.

(49) WSACS. WSACS Consensus Guidelines Summary. https://www.wsacs.org/education/436/wsacs-consensus-guidelines-summary/ (accessed on Apr 7, 2021).

(50) Cheng, H.-C.; Peng, B.-Y.; Chen, M.-S.; Huang, C.-F.; Lin, Y.; Shen, Y.-K. Influence of Deformation and Stress between Bone and Implant from Various Bite Forces by Numerical Simulation Analysis. *BioMed Res. Int.* **2017**, *2017*, 2827953.

(51) Knight, K. M.; King, G. E.; Palcsey, S. L.; Suda, A.; Liang, R.; Moalli, P. A. Mesh Deformation: A Mechanism Underlying Polypropylene Prolapse Mesh Complications In Vivo. *Acta Biomater.* **2022**, *148*, 323.

(52) Safshekan, F.; Tafazzoli-Shadpour, M.; Abdouss, M.; Shadmehr, M. B.; Ghorbani, F. Finite Element Simulation of Human Trachea: Normal vs. Surgically Treated and Scaffold Implanted Cases. *Int. J. Solids Struct.* **2020**, *190*, 35−46.

(53) Echeverria Molina, M. I.; Malollari, K. G.; Komvopoulos, K. Design Challenges in Polymeric Scaffolds for Tissue Engineering. *Front. Bioeng. Biotechnol.* **2021**, *9*, 9.